Optimization of Purcell-enhanced microcavities with the cylindrical finite-difference time-domain algorithm

N. W. E. Seet,* K. Dini, and T. C. H. Liew†
Division of Physics and Applied Physics, School of Physical and Mathematical Sciences, Nanyang Technological University, Singapore 637371

(Received 24 November 2023; revised 1 March 2024; accepted 20 March 2024; published 5 April 2024)

Quantum dots embedded in annular bullseye microcavities have been reported to be efficient single-photon sources. However, the proposed structures thus far often involve gratings of fixed periodicities, which may not be optimal considering the fact that Bessel functions are nonperiodic. In this paper, we present an optimization scheme for chirped annular microcavities where Purcell factors larger than 80 can be achieved through astute selection of the optimization function.

DOI: 10.1103/PhysRevA.109.043509

I. INTRODUCTION

Quantum technology proposals such as quantum computing [1–3] and quantum communication [4–6] rely strongly on the ability to engineer reliable high-quality efficient single-photon sources. To be operational, a prerequisite is that photons must be prepared into a single given quantum state, with well-defined time and space properties, in order for quantum effects such as quantum interference [7,8] and antibunching [9] to be observed. Many different platforms have been proposed to produce single photons including single atoms [10,11], single molecules [12], trapped ions [13], and quantum dots [14,15]. The main limitation in all these systems lies in the photon collection efficiency as well as in the emission rate of the source.

Quantum dots (QDs) have proven to be a reliable potential platform to support high-quality single-photon sources due to their possible incorporation into photonic systems and narrow spectral linewidth. In order to enhance the emission rate of a single-photon quantum dot emitter, one may either increase the quality of the optical system in which the QD is embedded or reduce the effective mode volume, i.e., confine the electromagnetic field in the vicinity of the QD. These effects can be achieved by carefully engineering the photonic structure around the QD [16–21].

A proposed solution involves fabrication of annular Bragg gratings obeying the second-order Bragg condition [22,23]. This specific way of engineering the nanostructure increases the spontaneous emission rate of the QD by modifying the neighboring environment and therefore both increasing the quality factor and reducing the mode volume. This is commonly known as the Purcell effect [24,25]. These annular Bragg gratings were shown to not only exhibit Purcell enhancement but also focus the QD's photon emission, along a direction in the far field and therefore improving the photon collection efficiency. However, if a structure has cylindrical symmetry, the radial solutions of the wave equation are represented as nonperiodic Bessel functions making the Bragg condition obsolete. Consequently, nonperiodic (or chirped) annular gratings have a high potential of improving the figures of merit (FOMs), such as Purcell factors and quality factors (Q factors), associated with the structure and therefore the quality of the single-photon source.

The chirped annular gratings have been shown to be ideal solutions for confining whispering gallery modes in annular structures [26,27]. However, for applications to single-photon sources, it is imperative that photons can be efficiently collected. That is, the out-of-plane scattering of electromagnetic fields must effectively produce a near Gaussian far field with low numerical aperture. The motivation behind the present paper, therefore, is the formulation of an optimization methodology, crafted to attain bullseye microcavities maximizing both the emission rate and the photon collection efficiency of a QD single-photon source.

First, we will introduce a self-developed finite-difference time-domain (FDTD) algorithm in cylindrical coordinates and discuss how using the azimuthal symmetry of the system can reduce our simulations to effectively two dimensions to reduce drastically the time of calculation. Second, we will elaborate how FOMs such as Purcell factors, Q factors, and effective mode volume are calculated with the algorithm. Then, we will show how a variation of the optimization function yields microcavities exhibiting different features. Finally we will show that by making a judicious choice of the optimization function, individuals can attain microcavities that exhibit properties tailored to their specific requirements.

II. FINITE-DIFFERENCE TIME-DOMAIN ALGORITHM IN CYLINDRICAL COORDINATES

The FDTD algorithm [28,29] is a rigorous computational method that evolves electromagnetic fields through Maxwell's equations. The FDTD algorithm's remarkable precision in describing the evolution of electromagnetic fields makes it an invaluable tool for studying a wide range of structures. Typically, the FDTD algorithm is constructed in Cartesian

*seet0075@e.ntu.edu.sg
†timothyliew@ntu.edu.sg

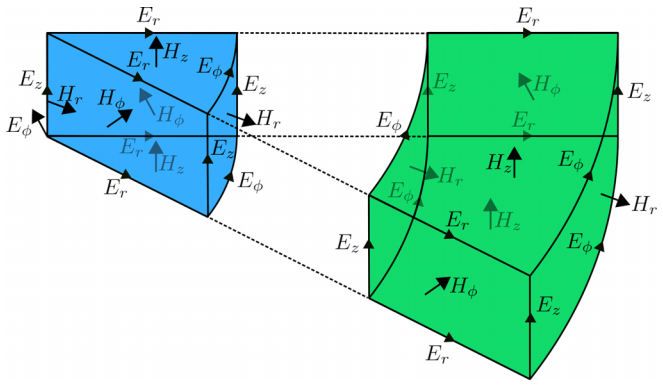

FIG. 1. Yee grid in cylindrical coordinates displaying the arrangement of the field components.

coordinates. However, the Cartesian scheme is not efficient in describing structures with curved geometries for two main reasons. First, a fine resolution on the curved edges of the structure is crucial to maintain the accuracy of the algorithm. With the time step being bounded by the Courant limit, the overall simulation time increases with finer grid resolution. Second, boundary conditions may remain inaccurate, despite having fine resolutions, owing to the "staircased" Cartesian grids. This motivates the study of the FDTD algorithm in cylindrical coordinates, which circumvents the aforementioned issues when analyzing structures of circular geometries.

Considering a source-free system, Maxwell's equation in a three-dimensional cylindrical coordinate system reads

$$\begin{aligned}
\frac{\partial E_r}{\partial t} &= \frac{1}{\epsilon}\left[\frac{1}{r}\frac{\partial H_z}{\partial \phi} - \frac{\partial H_\phi}{\partial z}\right],\\
\frac{\partial E_\phi}{\partial t} &= \frac{1}{\epsilon}\left[\frac{\partial H_r}{\partial z} - \frac{\partial H_z}{\partial r}\right],\\
\frac{\partial E_z}{\partial t} &= \frac{1}{\epsilon r}\left[\frac{\partial (rH_\phi)}{\partial r} - \frac{\partial H_r}{\partial \phi}\right],\\
\frac{\partial H_r}{\partial t} &= \frac{1}{\mu}\left[\frac{\partial E_\phi}{\partial z} - \frac{1}{r}\frac{\partial E_z}{\partial \phi}\right],\\
\frac{\partial H_\phi}{\partial t} &= \frac{1}{\mu}\left[\frac{\partial E_z}{\partial r} - \frac{\partial E_r}{\partial z}\right],\\
\frac{\partial H_z}{\partial t} &= \frac{1}{\mu r}\left[\frac{\partial E_r}{\partial \phi} - \frac{\partial (rE_\phi)}{\partial r}\right],
\end{aligned} \tag{1}$$

where $\epsilon = \epsilon_0\epsilon_r$ with ϵ_0 and ϵ_r being the permittivity of free space and relative permittivity of the material, respectively, and $\mu = \mu_0\mu_r$ with μ_0 and μ_r being the permeability of free space and relative permeability of the material, respectively. Similar to its Cartesian counterpart [30], the cylindrical coordinates FDTD algorithm also employs the half-gridding system called the Yee grid (Fig. 1). By definition, electromagnetic-field components are placed half a grid apart with electric fields located at the edges of a cell while magnetic fields are placed on the surfaces of the unit cell. This convention of field arrangement portrays Maxwell's curl equation that describes the generation of a magnetic flux from a circulating electric field and vice versa.

With Maxwell's equations and the Yee grid defined, one can discretize Eq. (1) and obtain the FDTD update equations. Special update equations are needed at the central point ($r = 0$) which we describe in the Appendix. If the structure of interest has azimuthal symmetry, a semianalytical method can be designed to reduce the FDTD algorithm to two dimensions via a method known as bodies of revolution (BOR) [29].

Bodies of revolution

To introduce the method of the BOR FDTD, we consider the following scenario. Suppose there are two different dipole orientations exciting the system. A vertically oriented dipole (z direction) will emit cylindrical waves exhibiting azimuthal symmetry but a horizontally oriented dipole will not since the fields are no longer emitted parallel to the r-ϕ plane. That is, while the structure has azimuthal symmetry, the corresponding photonic modes may not necessarily conform to the same symmetry, i.e., $\partial/\partial\phi_{\text{structure}} = 0$ but $\partial/\partial\phi_{\text{field}} \neq 0$ in general. Thus, to reduce the FDTD algorithm into two dimensions (r and z), a technique known as bodies of revolution is employed.

If a structure has azimuthal symmetry, it is natural to expand them as Fourier harmonics of the form

$$\begin{aligned}
\mathbf{E}(r,\phi,z) &= \sum_{m=0}^{\infty} \mathbf{E}_{u,m}\cos(m\phi) + \mathbf{E}_{v,m}\sin(m\phi),\\
\mathbf{H}(r,\phi,z) &= \sum_{m=0}^{\infty} \mathbf{H}_{u,m}\cos(m\phi) + \mathbf{H}_{v,m}\sin(m\phi),
\end{aligned} \tag{2}$$

where the Fourier coefficients $\mathbf{E}_{u,m}$, $\mathbf{E}_{v,m}$, $\mathbf{H}_{u,m}$, and $\mathbf{H}_{v,m}$ are functions of r and z. Substituting this directly into Eq. (1) yields two independent sets of two-dimensional Maxwell equations (Appendix A1) in r and z for a fixed azimuthal mode m. The first set of equations is

$$\begin{aligned}
\frac{\partial E_{r,v}}{\partial t} &= \frac{1}{\epsilon}\left[-\frac{m}{r}H_{z,u} - \frac{\partial H_{\phi,v}}{\partial z}\right],\\
\frac{\partial E_{\phi,u}}{\partial t} &= \frac{1}{\epsilon}\left[\frac{\partial H_{r,u}}{\partial z} - \frac{\partial H_{z,u}}{\partial r}\right],\\
\frac{\partial E_{z,v}}{\partial t} &= \frac{1}{\epsilon r}\left[\frac{\partial (rH_{\phi,v})}{\partial r} + mH_{r,u}\right],\\
\frac{\partial H_{r,u}}{\partial t} &= \frac{1}{\mu}\left[\frac{\partial E_{\phi,u}}{\partial z} - \frac{m}{r}E_{z,v}\right],\\
\frac{\partial H_{\phi,v}}{\partial t} &= \frac{1}{\mu}\left[\frac{\partial E_{z,v}}{\partial r} - \frac{\partial E_{r,v}}{\partial z}\right],\\
\frac{\partial H_{z,u}}{\partial t} &= \frac{1}{\mu r}\left[mE_{r,v} - \frac{\partial (rE_{\phi,u})}{\partial r}\right],
\end{aligned} \tag{3}$$

where the m dependence of the Fourier coefficients is taken to be implicit. If one is interested in multiple azimuthal modes, the algorithm has to be iterated for each mode. Nevertheless, the two-dimensional algorithm will retain its speed advantage over the three-dimensional counterpart. This is due to the algorithm's lower memory usage and the ability to employ larger time steps within the constraints of the Courant limit.

III. CHIRPED ANNULAR GRATINGS

Quantum dots embedded in annular Bragg gratings have been reported to behave as efficient single-photon sources [22,23,31]. The geometries of the structures are often chosen such that they obey the second-order Bragg condition. However, gratings with fixed periodicities may not be an optimal condition for annular structures. This is because radial solutions of the wave equation are Bessel functions which have nonperiodic zeros and do not obey Bloch's theorem. Consequently, gratings of varying periodicities could potentially improve important FOMs such as Purcell factors, quality factors (Q factors), effective mode volume, and collection efficiencies.

A study in [26,27] has shown that chirped annular gratings are indeed an optimal solution in confining whispering gallery modes. However, the proposed solution is not necessarily optimal for single-photon extraction since an out-of-plane scattering with near Gaussian far field is required for high collection efficiencies. Therefore, an alternative method is required and we have opted for a numerical approach.

A. Basic FDTD calculations

In theory, the Purcell Factor, F_p, of a microcavity can be approximated as [25]

$$F_p \approx \frac{3Q(\lambda_0/n)^3}{4\pi^2 V_{\text{eff}}} \tag{4}$$

where Q represents the Q factor; λ_0 represents the resonant cavity mode wavelength; n represents the refractive index of the cavity; V_{eff} represents the cavity's effective mode volume which is calculated with the expression

$$V_{\text{eff}} = \frac{\int_V \epsilon(\mathbf{r})|\mathbf{E}(\mathbf{r})|^2 d^3\mathbf{r}}{\max\{\epsilon(\mathbf{r})|\mathbf{E}(\mathbf{r})|^2\}} \tag{5}$$

where $\epsilon(\mathbf{r})$ represents the medium's relative permittivity and $\mathbf{E}(\mathbf{r})$ represents the electric field. The Purcell factor of a microcavity is described by the Q factor and the effective mode volume. These two quantities describe the temporal and spatial confinement of the field respectively. A larger Q factor leads to more interactions between the cavity mode and the quantum dot before leaking out of the structure; a smaller effective volume leads to stronger interactions between the cavity mode and the quantum dot. Combining these two effects will enhance the rate of spontaneous emission of the quantum dot, leading to larger Purcell factors.

While the Purcell factor may have a rather simple expression [Eq. (4)], the quantities involved are not easily predetermined. Nevertheless, the versatility of the FDTD algorithm enables efficient calculation of the Purcell factor and associated quantities by adhering to a few procedures.

The computational domain is illuminated with a horizontally oriented (r direction) electric dipole pulsed source placed in the middle of the cavity, exciting TE slab waves. Hence, we set $m = 1$ for all calculations as the fundamental mode of the cavity is of our main interest. The pulsed source, $S(t)$, takes the form of a Gaussian:

$$S(t) = A\exp\left(-\frac{(t-t_0)^2}{\tau}\right)\exp\left(-\frac{iE_0 t}{\hbar}\right) \tag{6}$$

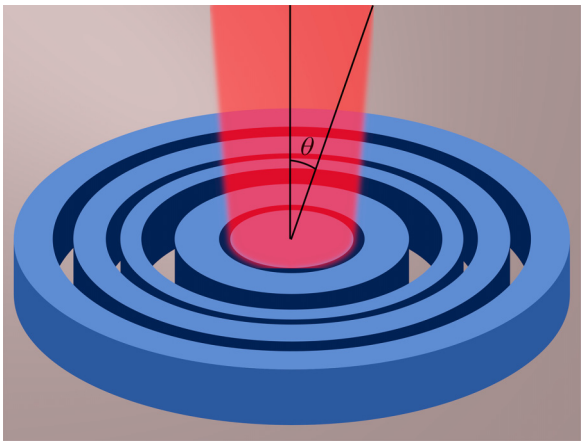

FIG. 2. Schematic of a (suspended) chirped bullseye cavity. θ represents the angle of emission.

where A is an arbitrary amplitude; $\tau \approx 0.97/\Delta f$, where Δf represents the frequency bandwidth of interest, is the pulse duration; $t_0 \approx 4.5\tau$ is a pulse delay to ensure that the algorithm detects a Gaussian signal; E_0 is the central energy of the Fourier-transformed pulse and $\hbar$ is the reduced Planck constant [28].

Fields penetrating through a surface area S, enclosing both the dipole and the structure (Fig. 2), are Fourier transformed in time to calculate the power emission spectrum, $P(\omega)$, which is prescribed by the Poynting integral as

$$P(\omega) = \frac{1}{2}\,\text{Re}\left\{\int_S [\widetilde{\mathbf{E}}(\mathbf{r},\omega) \times \widetilde{\mathbf{H}}^*(\mathbf{r},\omega)] \cdot d\mathbf{S}\right\} \tag{7}$$

where Re denotes taking the real part of the integral and ω represents the angular frequency. When calculating the power spectrum, it is vital that fields leaving surface S do not bounce back into the system, i.e., the fields escape to infinity. This is done by introducing perfectly matched layers (PMLs) on the edges of the computational domain to absorb fields as they penetrate through the PML interface [32].

By definition, the Purcell factor refers to an enhancement of spontaneous emission of a quantum dot in a cavity as compared to a homogeneous medium. Therefore, in the FDTD algorithm, the Purcell factor is calculated as

$$F_p(\omega) = \frac{P_{\text{cav}}(\omega)}{P_{\text{hom}}(\omega)} \tag{8}$$

where $P_{\text{cav}}(\omega)$ and $P_{\text{hom}}(\omega)$ denote the power spectrum measured with the structure and in a homogeneous medium respectively. In this particular case, the homogeneous medium is a simulation space filled entirely by the material of the cavity. With $F_p(\omega)$ at hand, the normalized power spectrum can be fitted with a Lorentzian model:

$$L(\omega) = \frac{A}{(\omega-\omega_0)^2 + (\Gamma/2)^2} + B \tag{9}$$

where ω_0 represents the resonant frequency; Γ represents the inverse lifetime; A and B are fitting parameters corresponding to the signal amplitude and background noise respectively. The Q factor of the cavity can be obtained as $Q = \omega_0/\Gamma$; the resonant wavelength can be obtained as $\lambda_0 = 2\pi c/\omega_0$, where

c represents the speed of light in free space; the Purcell factor can be interpolated as $F_p = L(\omega_0) = 4A/\Gamma^2 + B$.

B. Optimization process

With simulations running in the scale of minutes (computational time), the BOR-FDTD algorithm can be incorporated into an optimization algorithm to search for geometrical parameters.

Our annular microcavity consists of a suspended GaAs ($n \approx 3.53$) grating with geometrical parameters such as the central disk radius, trench width, groove width, and thickness to be determined. Each trench width and groove width are treated as an independent free variable. If the structure consists of N layers, there would be a total of $2N + 1$ degree of freedom (since the final groove width is assumed to stretch to infinity). When optimizing the geometrical parameters, it is crucial that they can be varied continuously in the optimization process. This can be achieved by implementing a nonuniform grid system [28,29].

Due to the large number of degrees of freedom, the particle swarm optimization (PSO) [33] was used to optimize our chirped microcavity system. Since the PSO is a stochastic method, the attained microcavity structure may differ for each run. Nevertheless, for a chosen optimization function, the inherent properties of the microcavity should remain similar.

The optimization function used in our simulations takes the form

$$M = \sum_i X_i w_i q_i \tag{10}$$

where q_i represents the FOM to be optimized, each being weighted by w_i with $\sum_i w_i = 1$; X_i is defined as

$$X_i = \begin{cases} -1 & \text{if } q_i \text{ needs to be maximized} \\ +1 & \text{if } q_i \text{ needs to be minimized} \end{cases}. \tag{11}$$

The choice of the optimization function in Eq. (10) allows us to prioritize on which q_i needs optimization by associating them with a larger w_i. Before defining the FOMs explicitly, we introduce the collection efficiency, C_{eff}, of the microcavity as

$$C_{\text{eff}}(\theta) = \frac{P_\theta}{P_{\text{tot}}} = \frac{\text{Re}\left\{\int_0^\theta \left[\mathbf{E}(\mathbf{r},t) \times \mathbf{H}^*(\mathbf{r},t)\right] \cdot d\mathbf{S}\right\}}{\text{Re}\left\{\int_{S_{\text{upp}}} \left[\mathbf{E}(\mathbf{r},t) \times \mathbf{H}^*(\mathbf{r},t)\right] \cdot d\mathbf{S}\right\}} \tag{12}$$

where θ represents the acceptance angle of the far-field emission (Fig. 2) and S_{upp} denotes an integral over the upper half of surface S. We considered only the upper half of the structure since the microcavities simulated have mirror symmetry in z.

In this paper, we choose to optimize four FOMs:

$$q_1 = \frac{Q}{Q_{\max}}, \tag{13}$$

$$q_2 = \frac{V_{\text{eff}}}{(\lambda_0/n)^3}, \tag{14}$$

$$q_3 = \frac{\int_{\text{cav}} |\mathbf{E}(\mathbf{r})|^2 d^3\mathbf{r}}{\int_{\text{str}} |\mathbf{E}(\mathbf{r})|^2 d^3\mathbf{r}}, \tag{15}$$

$$q_4 = \frac{\int \theta(C_{\text{eff}})\, dC_{\text{eff}}}{(\pi/2)\max(C_{\text{eff}})}, \tag{16}$$

with $X = [-1, +1, -1, +1]$. The FOMs defined from Eqs. (13)–(16) are normalized quantities to ensure that they have the same order of magnitude. This allows all the FOMs to be treated on an equal footing (or a footing defined solely by w_i).

In Eq. (13), q_1 represents the normalized quality factor and $Q_{\max}$ represents an upper bound on the quality factor. The value of $Q_{\max}$ can be increased accordingly if one wants a microcavity of higher quality factors. In Eq. (14), q_2 represents the normalized effective mode volume. In Eq. (15), q_3 represents the confinement factor of the microcavity defined as the total intensity in the central disk (or cavity) normalized to the total intensity in the entire structure. In Eq. (16), q_4 represents the average emission angle normalized to the maximum emission angle $\pi/2$. The integral in q_4 accounts for power emission from 0° to 90°. Thus, minimizing q_4 not only optimizes the emission angle but also mitigates potential side losses.

For application to experiments, the cavity mode of the nanostructure needs to be in resonance with the quantum dot. However, the FOMs defined in Eqs. (13)–(16) are independent of the quantum dot's resonance energy. Consequently, the energy of the cavity mode becomes arbitrary during the optimization process. This can be fixed easily by modifying the expression in Eq. (10) as

$$M' = \sum_i X_i w_i q_i + \Delta E' \quad \Delta E' = \frac{|E_0 - E_{\text{QD}}|}{E_{\text{QD}}} \tag{17}$$

where E_0 represents the simulated resonance energy of the trial microcavity and E_{QD} represents the resonance energy of the quantum dot. The quantity $\Delta E'$ is not treated as part of the q_is but rather as a fine tuning mechanism. Here, we set $E_{\text{QD}} = 1.347$ eV (around 920 nm).

IV. RESULTS AND DISCUSSION

Figure 3 shows four different structures attained with four different choices of M'. Structure A was attained with $w_1 = 1$, $w_2 = 0$, $w_3 = 0$, $w_4 = 0$, and $Q_{\max} = 600$. Structure B was attained with $w_1 = 0.5$, $w_2 = 0.5$, $w_3 = 0$, $w_4 = 0$, and $Q_{\max} = 600$. Structure C was attained with $w_1 = 0.1$, $w_2 = 0.5$, $w_3 = 0.2$, $w_4 = 0.2$, and $Q_{\max} = 600$. Structure D was attained with $w_1 = 0.05$, $w_2 = 0.5$, $w_3 = 0.2$, $w_4 = 0.25$, and $Q_{\max} = 300$. The steady-state field profiles of each structure are shown in Fig. 4. In Figs. 4(a), 4(d), 4(g), and 4(j) it is evident that half of the photons are emitted upwards and the other half are emitted downwards. This results in the collection efficiency being reduced by 50%. Nevertheless, the issue can be easily remedied by adding a substrate and a gold layer below the microcavity to redirect photons upwards [34].

From the steady-state field profiles shown in Fig. 4, it is evident that q_4 is crucial in obtaining a near Gaussian far field for high collection efficiencies. This is further illustrated with Fig. 5(b) where the collection efficiency curves of structures

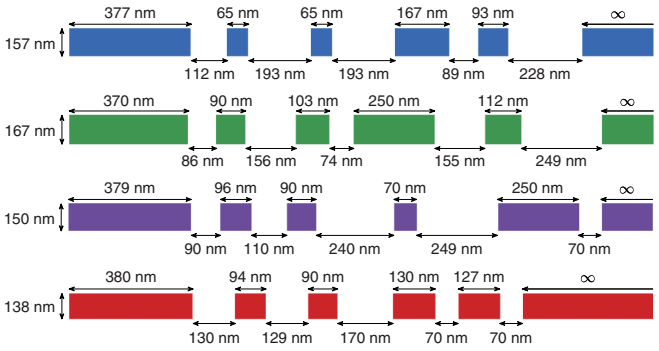

FIG. 3. Four different structures attained from the PSO algorithm. Structure A (blue; first) was attained with $w_1 = 1$, $w_2 = 0$, $w_3 = 0$, $w_4 = 0$, and $Q_{\max} = 600$. Structure B (green; second) was attained with $w_1 = 0.5$, $w_2 = 0.5$, $w_3 = 0$, $w_4 = 0$, and $Q_{\max} = 600$. Structure C (purple; third) was attained with $w_1 = 0.1$, $w_2 = 0.5$, $w_3 = 0.2$, $w_4 = 0.2$, and $Q_{\max} = 600$. Structure D (red; fourth) was attained with $w_1 = 0.05$, $w_2 = 0.5$, $w_3 = 0.2$, $w_4 = 0.25$, and $Q_{\max} = 300$.

A and B are well below those of structures C and D. In addition, Fig. 5(e) shows that the average emission angles of structure A and B are approximately 49° and 40° respectively as compared to structure C which has an average emission

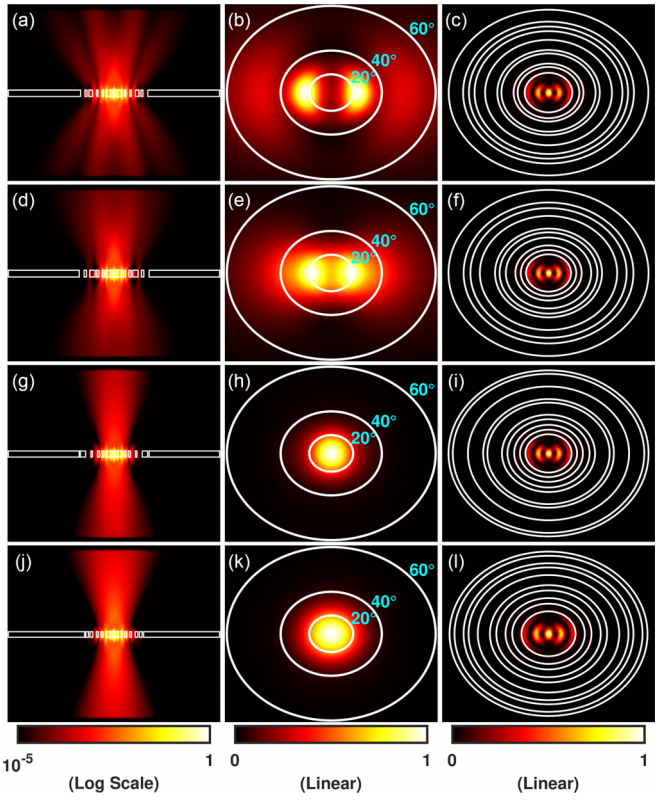

FIG. 4. Figure showing the steady-state fields (with normalized intensities) of structure A (a–c), structure B (d–f), structure C (g–i), and structure D (j–l). (a), (d), (g), (j) Emission field profiles in the x-z plane plotted in the logarithmic scale for clarity. (b), (e), (h), (k) Far-field profiles in the horizontal plane. (c), (f), (i), (l) In-plane dipole emission at the position of the dipole source.

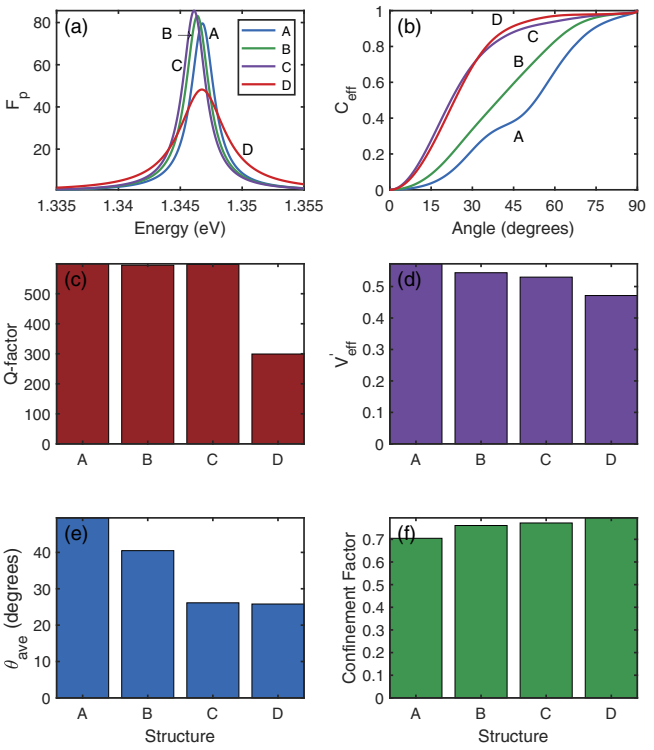

FIG. 5. Plots summarizing data and FOMs obtained from the four structures. (a) Purcell factor as a function of energy (in eV). (b) Collection efficiency against acceptance angle. (c) Comparison of Q factors attained. (d) Comparison of the normalized effective mode volume $V'_{\text{eff}} = V_{\text{eff}}/(\lambda_0/n)^3$. (e) Comparison of the average angle of emission calculated with the expression for q_4 in Eq. (16) (neglecting the $\pi/2$ at the denominator). (e) Comparison of the confinement factor calculated with Eq. (15).

angle of about 25°. Thus, even though structures A, B, and C have similar Purcell factors of $F_p \approx 80$ [Fig. 5(a)], we consider structure C as superior for applications to single-photon extraction due to its larger collection efficiency.

With a large Q factor of $Q \approx 600$, the Purcell factor of structure C ($F_p \approx 82$) is almost four times larger as compared to previously reported results of $F_p \approx 20$, $V'_{\text{eff}} \approx 1.5$, and $Q \approx 200$ [22,34]. While this result shows that chirped gratings indeed allow us to achieve larger Purcell factors as compared to the standard design with fixed periodicities, a large Q factor (small linewidth) leaves smaller room for errors in experiments as the cavity mode needs to be precisely tuned to be in resonance with the quantum dot. In light of this, the w_is were modified slightly and the upper bound on the quality factor was lowered to $Q_{\max} = 300$ to attain structure D. Figure 4(k) shows that structure D has a near Gaussian far-field profile with collection efficiency curves almost matching those of structure C [Fig. 5(b)] and an emission angle similar to that of structure C [Fig. 5(e)]. Even though the Q factor of structure C is two times that of structure D, the Purcell factor of structure D ($F_p \approx 45$) is slightly larger than half that of structure C ($F_p \approx 82$). This is due to the lower effective mode volume of structure D as compared to structure C [Fig. 5(d)]. Despite the lower Purcell factor of structure D as compared to structure C, it is still an improvement from past results. This shows that

chirped annular gratings not only improve the results obtained in the past, but also allow users to design microcavities that are tailored to their own needs or experimental limitations.

The quantity q_3 or confinement factor is introduced to ensure that the central disk plays the role of a cavity where a large fraction of the intensity resides within the central disk. In Fig. 5(f), it is apparent that the inclusion of q_3 in M allows a larger intensity to be confined within the cavity (≈80%).

V. CONCLUSION

Overall, the optimization scheme presented has shown success in attaining chirped annular microcavities that improve figure of merit of current annular grating structures. For instance, a higher Purcell factor was obtained without sacrifice of the collection efficiency. In addition, with direct control of the w_is and the freedom to define the q_is [Eq. (10)], users will be able to design structures that exhibit properties suited to their own requirements. It is therefore evident that the optimization scheme presented here is versatile, making it a potential tool for optimizing a wide range of photonic structures.

ACKNOWLEDGMENT

This work was supported by the Singaporean Ministry of Education via AcRF Tier 2 Project No. MOE-T2EP50121-0020.

APPENDIX

1. Bodies of revolution derivation

We start our derivation from substituting Eq. (2) into Eq. (1).

Collecting $\cos(m\phi)$ terms,

$$\begin{aligned}
\frac{\partial E_{r,u}}{\partial t} &= \frac{1}{\epsilon}\left[\frac{m}{r}H_{z,v} - \frac{\partial H_{\phi,u}}{\partial z}\right],\\
\frac{\partial E_{\phi,u}}{\partial t} &= \frac{1}{\epsilon}\left[\frac{\partial H_{r,u}}{\partial z} - \frac{\partial H_{z,u}}{\partial r}\right],\\
\frac{\partial E_{z,u}}{\partial t} &= \frac{1}{\epsilon r}\left[\frac{\partial (rH_{\phi,u})}{\partial r} - mH_{r,v}\right],\\
\frac{\partial H_{r,u}}{\partial t} &= \frac{1}{\mu}\left[\frac{\partial E_{\phi,u}}{\partial z} - \frac{m}{r}E_{z,v}\right],\\
\frac{\partial H_{\phi,u}}{\partial t} &= \frac{1}{\mu}\left[\frac{\partial E_{z,u}}{\partial r} - \frac{\partial E_{r,u}}{\partial z}\right],\\
\frac{\partial H_{z,u}}{\partial t} &= \frac{1}{\mu r}\left[mE_{r,v} - \frac{\partial (rE_{\phi,u})}{\partial r}\right].
\end{aligned} \tag{A1}$$

Collecting $\sin(m\phi)$ terms,

$$\begin{aligned}
\frac{\partial E_{r,v}}{\partial t} &= \frac{1}{\epsilon}\left[-\frac{m}{r}H_{z,u} - \frac{\partial H_{\phi,v}}{\partial z}\right],\\
\frac{\partial E_{\phi,v}}{\partial t} &= \frac{1}{\epsilon}\left[\frac{\partial H_{r,v}}{\partial z} - \frac{\partial H_{z,v}}{\partial r}\right],\\
\frac{\partial E_{z,v}}{\partial t} &= \frac{1}{\epsilon r}\left[\frac{\partial (rH_{\phi,v})}{\partial r} + mH_{r,u}\right],\\
\frac{\partial H_{r,v}}{\partial t} &= \frac{1}{\mu}\left[\frac{\partial E_{\phi,v}}{\partial z} + \frac{m}{r}E_{z,u}\right],\\
\frac{\partial H_{\phi,v}}{\partial t} &= \frac{1}{\mu}\left[\frac{\partial E_{z,v}}{\partial r} - \frac{\partial E_{r,v}}{\partial z}\right],\\
\frac{\partial H_{z,v}}{\partial t} &= \frac{1}{\mu r}\left[-mE_{r,u} - \frac{\partial (rE_{\phi,v})}{\partial r}\right].
\end{aligned} \tag{A2}$$

From Eqs. (A1) and (A2), it is evident that the equations involving the fields $E_{r,v}$, $E_{\phi,u}$, $E_{z,v}$, $H_{r,u}$, $H_{\phi,v}$, and $H_{z,u}$ are decoupled from the equations involving the other six field components. Thus, two sets of six equations are obtained.

The first set (involving fields $E_{r,v}$, $E_{\phi,u}$, $E_{z,v}$, $H_{r,u}$, $H_{\phi,v}$, and $H_{z,u}$) is

$$\begin{aligned}
\frac{\partial E_{r,v}}{\partial t} &= \frac{1}{\epsilon}\left[-\frac{m}{r}H_{z,u} - \frac{\partial H_{\phi,v}}{\partial z}\right],\\
\frac{\partial E_{\phi,u}}{\partial t} &= \frac{1}{\epsilon}\left[\frac{\partial H_{r,u}}{\partial z} - \frac{\partial H_{z,u}}{\partial r}\right],\\
\frac{\partial E_{z,v}}{\partial t} &= \frac{1}{\epsilon r}\left[\frac{\partial (rH_{\phi,v})}{\partial r} + mH_{r,u}\right],\\
\frac{\partial H_{r,u}}{\partial t} &= \frac{1}{\mu}\left[\frac{\partial E_{\phi,u}}{\partial z} - \frac{m}{r}E_{z,v}\right],\\
\frac{\partial H_{\phi,v}}{\partial t} &= \frac{1}{\mu}\left[\frac{\partial E_{z,v}}{\partial r} - \frac{\partial E_{r,v}}{\partial z}\right],\\
\frac{\partial H_{z,u}}{\partial t} &= \frac{1}{\mu r}\left[mE_{r,v} - \frac{\partial (rE_{\phi,u})}{\partial r}\right].
\end{aligned} \tag{A3}$$

The second set (involving fields $E_{r,u}$, $E_{\phi,v}$, $E_{z,u}$, $H_{r,v}$, $H_{\phi,u}$, and $H_{z,v}$) is

$$\begin{aligned}
\frac{\partial E_{r,u}}{\partial t} &= \frac{1}{\epsilon}\left[\frac{m}{r}H_{z,v} - \frac{\partial H_{\phi,u}}{\partial z}\right],\\
\frac{\partial E_{\phi,v}}{\partial t} &= \frac{1}{\epsilon}\left[\frac{\partial H_{r,v}}{\partial z} - \frac{\partial H_{z,v}}{\partial r}\right],\\
\frac{\partial E_{z,u}}{\partial t} &= \frac{1}{\epsilon r}\left[\frac{\partial (rH_{\phi,u})}{\partial r} - mH_{r,v}\right],\\
\frac{\partial H_{r,v}}{\partial t} &= \frac{1}{\mu}\left[\frac{\partial E_{\phi,v}}{\partial z} + \frac{m}{r}E_{z,u}\right],\\
\frac{\partial H_{\phi,u}}{\partial t} &= \frac{1}{\mu}\left[\frac{\partial E_{z,u}}{\partial r} - \frac{\partial E_{r,u}}{\partial z}\right],\\
\frac{\partial H_{z,v}}{\partial t} &= \frac{1}{\mu r}\left[-mE_{r,u} - \frac{\partial (rE_{\phi,v})}{\partial r}\right].
\end{aligned} \tag{A4}$$

Since the two sets of equations above are independent from one another, we may choose to only discretize either (A3) or (A4) to form the FDTD update equations. This is because choosing one over the other merely results in a 90° rotation of the fields due to a different choice of basis representation. However, when the material of interest is anisotropic, the fields from Eqs. (A3) and (A4) will couple with one another and no longer be independent.

As discussed in the main text, the fields are positioned according to the Yee grid (Fig. 1). On top of the field components being half a grid apart in space, magnetic fields are

defined to be updated at half-integer time steps $(n+1/2)$ while electric fields are updated at integer time steps (n). This is a consequence of having two coupled fields propagating together at the same time, but only one field can be updated before the other in the algorithm. As a result, the conventional choice in the FDTD algorithm is to update the magnetic fields first. Discretizing the first set of equations [Eq. (A3)] with the central finite-difference scheme, the FDTD update equations are obtained as (i and k indexes the r and z components respectively; the superscript n denotes the time step; $r_{i+1/2} = r_i + \Delta r/2$)

$$H_{r,u}^{n+\frac{1}{2}}(i,k) = H_{r,u}^{n-\frac{1}{2}}(i,k) + \frac{\Delta t}{\mu}\left[\frac{E_\phi^n(i,k+1) - E_\phi^n(i,k)}{\Delta z} - \frac{mE_z^n(i,k)}{r_i}\right], \tag{A5}$$

$$H_{\phi,v}^{n+\frac{1}{2}}(i,k) = H_{\phi,v}^{n-\frac{1}{2}}(i,k) + \frac{\Delta t}{\mu}\left[\frac{E_{z,v}^n(i+1,k) - E_{z,v}^n(i,k)}{\Delta r} - \frac{E_{r,v}^n(i,k+1) - E_{r,v}^n(i,k)}{\Delta z}\right], \tag{A6}$$

$$H_{z,u}^{n+\frac{1}{2}}(i,k) = H_{z,u}^{n-\frac{1}{2}}(i,k) + \frac{\Delta t}{\mu r_{i+\frac{1}{2}}}\left[mE_{r,v}^n - \frac{r_{i+1}E_{\phi,u}^n(i+1,k) - r_iE_{\phi,u}^n(i,k)}{\Delta r}\right], \tag{A7}$$

$$E_{r,v}^{n+1}(i,k) = E_{r,v}^n(i,k) + \frac{\Delta t}{\epsilon}\left[-\frac{mH_{z,u}^{n+\frac{1}{2}}(i,k)}{r_{i+\frac{1}{2}}} - \frac{H_{\phi,v}^{n+\frac{1}{2}}(i,k) - H_{\phi,v}^{n+\frac{1}{2}}(i,k-1)}{\Delta z}\right], \tag{A8}$$

$$E_{\phi,u}^{n+1}(i,k) = E_{\phi,u}^n(i,k) + \frac{\Delta t}{\epsilon}\left[\frac{H_{r,u}^{n+\frac{1}{2}}(i,k) - H_{r,u}^{n+\frac{1}{2}}(i,k-1)}{\Delta z} - \frac{H_{z,u}^{n+\frac{1}{2}}(i,k) - H_{z,u}^{n+\frac{1}{2}}(i-1,k)}{\Delta r}\right], \tag{A9}$$

$$E_{z,v}^{n+1}(i,k) = E_{z,v}^n(i,k) + \frac{\Delta t}{r_i\epsilon}\left[\frac{r_{i+\frac{1}{2}}H_{\phi,v}^{n+\frac{1}{2}}(i,k) - r_{i-\frac{1}{2}}H_{\phi,v}^{n+\frac{1}{2}}(i-1,k)}{\Delta r} + mH_{r,u}^{n+\frac{1}{2}}(i,k)\right]. \tag{A10}$$

2. On-axis updates for E_z, E_ϕ, and H_r

An unavoidable consequence of the central finite-differencing scheme is the existence of nonupdatable points. These points lie on the boundary nodes, i.e., $\alpha = 1$ or N_α, where $\alpha = \{i, j, k\}$ and N_α denotes the total number of points in a particular direction. For example, when $i = 1$ is substituted into Eq. (A9), the term $H_{z,u}^{n+1/2}(0,k)$, which does not exist, is required. This does not create complications in the Cartesian scheme since computational domains are typically truncated with PMLs which extend a few cells away from the boundary. However, in cylindrical coordinates, the boundary computational node at $i = 1$ represents $r = 0$ that sits at the center of the grid space. If the update at this point is neglected, it effectively translates to a nonphysical effect where a Dirichlet boundary is present at the center of the computational domain. Therefore, it is imperative that field components affected by such boundary nonupdatability are specially treated.

The fields that require these special updates lie on the $r = 0$ axis, namely E_z, E_ϕ, and H_r. E_z is only nonzero when $m = 0$ while E_ϕ and H_r are only nonzero when $m = 1$. While it is crucial that E_z on the axis has to be updated whenever necessary, the special updates for E_ϕ and H_r are optional. This is because $E_z(1,k)$ is coupled into Eq. (A6) while the other two on-axis fields, $E_\phi(1,k)$ and $H_r(1,k)$, do not couple to any of the FDTD updating equations. For instance, although $E_\phi(1,k)$ couples to $H_z(1,k)$ in Eq. (A7), it is multiplied by $r_1 = 0$. On the other hand, $H_r(1,k)$ does not couple to the standard updates in Eqs. (A9) and (A10). This is because of the r derivatives present in the E_ϕ and E_z updates that fail to work at the boundaries ($i = 1$). Nevertheless, updating E_ϕ and H_r at $r = 0$ may still be useful in analyzing field profiles.

a. E_z special update ($m = 0$)

For the E_z on-axis update, consider the integral form of Maxwell's equations:

$$\oint_C \mathbf{H}\cdot d\mathbf{l} = \oint_S \epsilon\frac{\partial \mathbf{E}}{\partial t}\cdot d\mathbf{S}. \tag{A11}$$

If $m \neq 0$, the closed loop integral of $\mathbf{H}$ will be zero. Thus, the E_z on-axis update is only necessary whenever $m = 0$. From here on, we assume $m = 0$ and derive the required update equation:

$$H_\phi\Big|_{\frac{1}{2},k+\frac{1}{2}}^{n+\frac{1}{2}}\left(2\pi r_{\frac{1}{2}}\right) = \epsilon\frac{\partial E_z}{\partial t}\Big|_{0,k+\frac{1}{2}}^{n+\frac{1}{2}}\left(\pi r_{\frac{1}{2}}^2\right). \tag{A12}$$

Writing $r_{\frac{1}{2}} = \Delta r/2$, the on-axis E_z update equation reads

$$E_z\Big|_{0,k+\frac{1}{2}}^{n+1} = E_z\Big|_{0,k+\frac{1}{2}}^{n} + \frac{4\Delta t}{\epsilon\Delta r}H_\phi\Big|_{\frac{1}{2},k+\frac{1}{2}}^{n+\frac{1}{2}}. \tag{A13}$$

This is written computationally as

$$E_z^{n+1}(1,k) = E_z^n(1,k) + \frac{4\Delta t}{\epsilon\Delta r}H_\phi^{n+\frac{1}{2}}(1,k). \tag{A14}$$

b. E_ϕ special update ($m = 1$)

The E_ϕ special update equation can be obtained using a similar method done with E_z. The contour chosen now will be along the r-z plane, enclosed by H_r and H_z:

$$\frac{\Delta r}{2}\left[H_r\Big|_{0,k+\frac{1}{2}}^{n+\frac{1}{2}} - H_r\Big|_{0,k-\frac{1}{2}}^{n+\frac{1}{2}}\right] - \Delta z H_z\Big|_{\frac{1}{2},k}^{n+\frac{1}{2}} = \epsilon\Delta z\frac{\Delta r}{2}\frac{\partial E_\phi}{\partial t}\Big|_{0,k}^{n+\frac{1}{2}}. \tag{A15}$$

Rearranging gives the E_ϕ special update equation

$$E_\phi\Big|_{0,k}^{n+1} = E_\phi\Big|_{0,k}^{n} - \frac{2\Delta t}{\epsilon \Delta r} H_z\Big|_{\frac{1}{2},k}^{n+\frac{1}{2}} + \frac{\Delta t}{\epsilon \Delta z}\left[H_r\Big|_{0,k+\frac{1}{2}}^{n+\frac{1}{2}} - H_r\Big|_{0,k-\frac{1}{2}}^{n+\frac{1}{2}} \right]. \tag{A16}$$

This is written computationally as

$$E_\phi^{n+1}(1,k) = E_\phi^{n}(1,k) - \frac{2\Delta t}{\epsilon \Delta r} H_z^{n+\frac{1}{2}}(1,k) + \frac{\Delta t}{\epsilon \Delta z}\left[H_r^{n+\frac{1}{2}}(1,k) - H_r^{n+\frac{1}{2}}(1,k-1) \right]. \tag{A17}$$

c. H_r special update ($m = 1$)

For the H_r special update, the integral form is not required since there is no r derivative term in the standard updating equation. Immediately using Eq. (A5) and using the value of E_z at $r = \Delta r$ as an approximation (since $E_z = 0$ on the axis if $m \neq 0$), the H_r special update equation is obtained as

$$H_r^{n+\frac{1}{2}}(1,k) = H_r^{n-\frac{1}{2}}(1,k) - \frac{\Delta t}{\mu \Delta r} E_z^{n}(2,k) + \frac{\Delta t}{\mu \Delta z}\left[E_\phi^{n}(1,k+1) - E_\phi^{n}(1,k) \right]. \tag{A18}$$

3. Pareto front optimization

In Sec. III B, we demonstrated the optimization of chirped annular microcavities and illustrated how distinct choices of optimization functions yield different geometrical parameters, each exhibiting its own unique properties (Figs. 4 and 5). The optimization scheme outlined in Sec. III B was based on the implementation of the PSO algorithm that generates structures exhibiting Purcell factors surpassing those obtained by previous schemes for periodic gratings [22,34]. To support the assertion that chirped gratings are superior, we conducted an additional optimization by the construction of a Pareto front.

The Pareto front is defined as a set of nondominated solutions. That is, there are no structures in the parameter space that can improve all FOMs located at the Pareto front simultaneously. For example, suppose there are two general FOMs to be optimized η_1 and η_2. In our case, η_1 represents the Purcell factor (to be maximized) and η_2 represents the emission angle (to be minimized). A structure with FOMs η_1 and η_2 lies on the Pareto front if there are no alternative structures such that $\eta_1' > \eta_1$ and $\eta_2' < \eta_2$ simultaneously where η_1' and η_2' represent the Purcell factor and emission angle of an alternative (general) structure in the parameter space respectively.

The PSO algorithm was executed multiple times with the optimization function being

$$M = \frac{\eta_1 \eta_3 \eta_4}{\eta_2} \tag{A19}$$

where

$$\eta_1 = F_p(\omega_0), \tag{A20}$$

$$\eta_2 = \frac{\int \theta(C_{\text{eff}})\, dC_{\text{eff}}}{\max(C_{\text{eff}})}, \tag{A21}$$

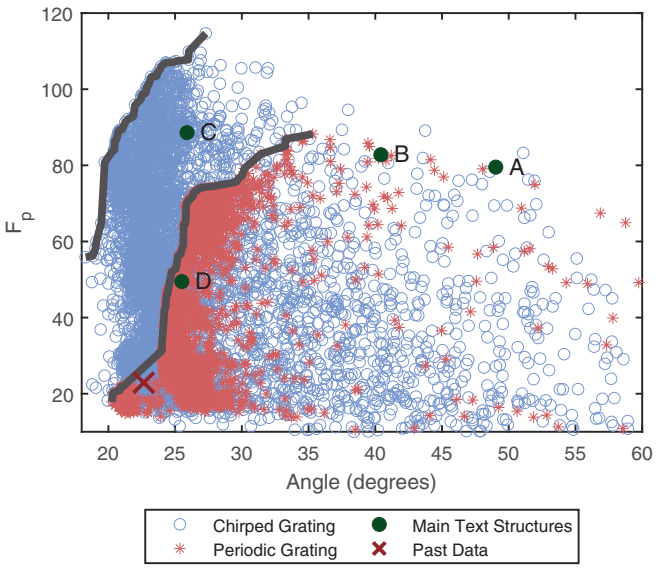

FIG. 6. A Pareto front (black outlines) interpolation based on multiple runs of the PSO algorithm. Each individual iteration is represented by different symbols as shown in the legend. The optimized structures from both the main text and an existing periodic structure [34] are included as well.

$$\eta_3 = \frac{\int_{\text{cav}} |\mathbf{E}(\mathbf{r})|^2 d^3\mathbf{r}}{\int_{\text{str}} |\mathbf{E}(\mathbf{r})|^2 d^3\mathbf{r}}, \tag{A22}$$

$$\eta_4 = \int |\widetilde{\mathbf{E}}(\mathbf{r}, z_0)|^2 \widetilde{G}(\mathbf{r})\, d^2\mathbf{r}. \tag{A23}$$

η_1 represents the Purcell factor at the resonance frequency ω_0; η_2 represents the average angle, similar to the expression of q_4 in Eq. (16); η_3 represents the field confinement factor, similar to the expression of q_3 in Eq. (15); η_4 represents an overlap integral of the far-field intensity at z_0 with a Gaussian function $G(\mathbf{r})$. The tilde signs on the expression in Eq. (A23) indicate that the functions are normalized, ensuring that the overlap integral is between 0 and 1 and amplitude independent. We note here that the optimization function in Eq. (A19) is independent of the Purcell factor's resonance energy [as compared to Eq. (17)]. This lifts off a constraint on the optimization function, opening up the potential for achieving higher Purcell factors and lower emission angles. An additional rescaling to the structural geometry can be done to fine tune the energy peak of the Purcell factor without impact on any of the FOMs.

After multiple executions of the PSO algorithm for both chirped and periodic gratings, a Pareto front was constructed on the scattered plot, consisting of all the swarm parameters, highlighted by the black outlines in Fig. 6. In addition, we verified that all the points on the Pareto front and structures C and D have an overlap integral [Eq. (A23)] of larger than 99%. We further compared our results obtained with results obtained in [34] for a periodic grating (shown as a red cross in Fig. 6). Even though periodic structures can yield Purcell factors exceeding 20, the utilization of chirped gratings offers the potential for achieving higher Purcell factors with smaller emission angles.

[1] P. Kok, W. J. Munro, K. Nemoto, T. C. Ralph, J. P. Dowling, and G. J. Milburn, Rev. Mod. Phys. **79**, 797(E) (2007).

[2] H.-S. Zhong, H. Wang, Y.-H. Deng, M.-C. Chen, L.-C. Peng, Y.-H. Luo, J. Qin, D. Wu, X. Ding, Y. Hu *et al.*, Science **370**, 1460 (2020).

[3] S. Aaronson and A. Arkhipov, in *Proceedings of the Forty-Third Annual ACM Symposium on Theory of Computing (STOC'11)* (Association for Computing Machinery, New York, NY, 2011), p. 333.

[4] Z. Qi, Y. Li, Y. Huang, J. Feng, Y. Zheng, and X. Chen, Light Sci. Appl. **10**, 183 (2021).

[5] C. Schimpf *et al.*, Sci. Adv. **7**, eabe8905 (2021).

[6] J. Yin *et al.*, Science **356**, 1140 (2017).

[7] C. K. Hong, Z. Y. Ou, and L. Mandel, Phys. Rev. Lett. **59**, 2044 (1987)

[8] H. Ollivier, S. E. Thomas, S. C. Wein, I. Maillette de Buy Wenniger, N. Coste, J. C. Loredo, N. Somaschi, A. Harouri, A. Lemaitre, I. Sagnes, L. Lanco, C. Simon, C. Anton, O. Krebs, and P. Senellart, Phys. Rev. Lett. **126**, 063602 (2021).

[9] H. Paul, Rev. Mod. Phys. **54**, 1061 (1982).

[10] D. B. Higginbottom *et al.*, New J. Phys. **18**, 093038 (2016).

[11] M. Hijlkema, B. Weber, H. Specht *et al.*, Nature Phys **3**, 253 (2007).

[12] B. Lounis and W. E. Moerner, Nature (London) **407**, 491 (2000).

[13] N. Piro, F. Rohde, C. Schuck, M. Almendros, J. Huwer, J. Ghosh, A. Haase, M. Hennrich, F. Dubin, and J. Eschner, Nat. Phys. **7**, 17 (2011).

[14] P. Senellart, G. Solomon, and A. White, Nat. Nanotechnol. **12**, 1026 (2017).

[15] J. Claudon *et al.*, Nature Photon **4**, 174 (2010).

[16] H. Wang, H. Hu, T.-H. Chung, J. Qin, X. Yang, J.-P. Li, R.-Z. Liu, H.-S. Zhong, Y.-M. He, X. Ding, Y.-H. Deng, Q. Dai, Y.-H. Huo, S. Höfling, C.-Y. Lu, and J.-W. Pan, Phys. Rev. Lett. **122**, 113602 (2019).

[17] H. Wang *et al.*, Nat. Photonics **13**, 770 (2019).

[18] S. Jun, J. Kim, M. Choi, B. Su Kim, J. Park, D. Kim, B. Shin, and Y.-H. Cho, ACS Nano **18**, 1396 (2024).

[19] P. Michler, A. Kiraz, C. Becher, W. V. Schoenfeld, P. M. Petroff, L. Zhang, E. Hu, and A. Imamoglu, Science **290**, 2282 (2000).

[20] A. Shields, Nature Photon **1**, 215 (2007).

[21] C. Santori, M. Pelton, G. Solomon, Y. Dale, and Y. Yamamoto, Phys. Rev. Lett. **86**, 1502 (2001).

[22] M. Davanço, M. T. Rakher, D. Schuh, A. Badolato, and K. Srinivasan, Appl. Phys. Lett. **99**, 041102 (2011).

[23] X. Chen, R. Su, J. Liu, J. Li, and X.-H. Wang, Photon. Res. **10**, 2066 (2022).

[24] E. M. Purcell, Spontaneous emission probabilities at radio frequencies, in *Confined Electrons and Photons*, edited by E. Burstein and C. Weisbuch, NATO ASI Series, Vol. 340 (Springer, New York, 1995).

[25] J.-M. Gerard and B. Gayral, J. Lightwave Technol. **17**, 2089 (1999).

[26] L. Djaloshinski and M. Orenstein, IEEE J. Quantum Electron. **35**, 737 (1999).

[27] J. Scheuer and A. Yariv, J. Opt. Soc. Am. B **20**, 2285 (2003).

[28] A. Z. Elsherbeni and V. Demir, *The Finite-Difference Time-Domain in Electromagnetics*, 2nd ed. (Institution of Engineering and Technology, UK, 2014).

[29] A. Taflove and S. Hagness, *Computational Electrodynamics: The Finite-Difference Time-Domain Method*, 3rd ed. (Artech House, Boston, 2005).

[30] K. Yee, IEEE Trans. Antennas Propag. **14**, 302 (1966).

[31] W. Li, L. Morales-Inostroza, W. Xu, P. Zhang, J. Renger, S. Götzinger, and X.-W. Chen, ACS Photonics **7**, 2474 (2020).

[32] J. A. Roden and S. D. Gedney, Microw. Opt. Technol. Lett. **27**, 334 (2000).

[33] J. Kennedy and R. Eberhart, in *Proceedings of the ICNN'95 International Conference on Neural Networks, Perth,WA, Australia* (IEEE, Piscataway, NJ, 1995), pp. 1942–1948.

[34] J. Liu *et al.*, Nat. Nanotechnol. **14**, 586 (2019).